Appl Phys B (2012) 107:529–538
DOI 10.1007/s00340-012-5051-4

Applied Physics B
Lasers and Optics

CO_2^* chemiluminescence study at low and elevated pressures

M. Kopp · M. Brower · O. Mathieu · E. Petersen · F. Güthe

Received: 22 March 2012 / Revised version: 6 April 2012 / Published online: 26 May 2012

Abstract Chemiluminescence experiments have been performed to assess the state of current CO_2^* kinetics modeling. The difficulty with modeling CO_2^* lies in its broad emission spectrum, making it a challenge to isolate it from background emission of species such as CH^* and CH_2O^*. Experiments were performed in a mixture of $0.0005H_2 + 0.01N_2O + 0.03CO + 0.9595Ar$ in an attempt to isolate CO_2^* emission. Temperatures ranged from 1654 K to 2221 K at two average pressures, 1.4 and 10.4 atm. The unique time histories of the various chemiluminescence species in the unconventional mixture employed at these conditions allow for easy identification of the CO_2^* concentration. Two different wavelengths to capture CO_2^* were used; one optical filter was centered at 415 nm and the other at 458 nm. The use of these two different wavelengths was done to verify that broadband CO_2^* was in fact being captured, and not emission from other species such as CH^* and CH_2O^*. As a baseline for time history and peak magnitude comparison, OH^* emission was captured at 307 nm simultaneously with the two CO_2^* filters. The results from the two CO_2^* filters were consistent with each other, implying that indeed the same species (i.e., CO_2^*) was being measured at both wavelengths. A first-generation kinetics model for CO_2^* and CH_2O^* was developed, since no comprehensively validated one exists to date. CH_2O^* and CH^* were ruled out as being present in the experiments at any measurable level, based on calculations and comparisons with the data. Agreement with the CO_2^* model was only fair, which necessitates future improvements for a better understanding of CO_2^* chemiluminescence as well as the kinetics of the ground state species.

1 Introduction

Chemiluminescence measurements play an important role in gas turbine health monitoring as a simple, cost-effective optical diagnostic [1]. Sample species include OH^*, CH^*, and CO_2^*, among others. Shock-tube measurements of these species can also play a key role in kinetics model validation, but it is sometimes difficult to isolate certain species in the hydrocarbon system due to a broadband background in the hydrocarbon chemiluminescence spectrum, shown in Fig. 1.

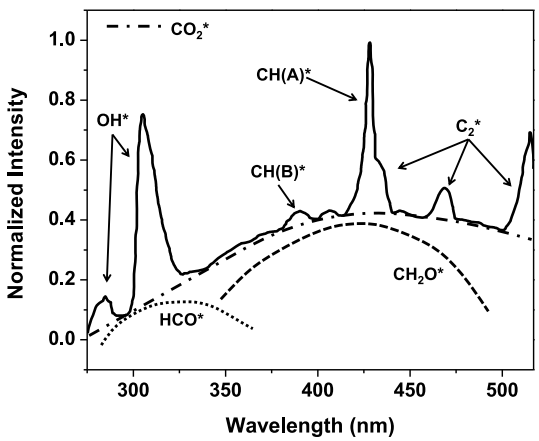

Fig. 1 Recreation of chemiluminescence spectrum showing the broadband background of the hydrocarbon chemiluminescence from CO_2^*, HCO^*, and CH_2O^*, based on work from [2, 3, 5, 6, 14]. Note that this portion does not cover the entire range of CO_2^* emission as suggested by [14]

M. Kopp · M. Brower · O. Mathieu · E. Petersen (✉)
Department of Mechanical Engineering, Texas A&M University, College Station, TX, USA
e-mail: epetersen@tamu.edu

F. Güthe
Combustion Technology Group, Alstom Power, Brown Boveri Strasse 7, 5401 Baden, Switzerland

In most gas turbine applications, CO_2^* is believed to be the main species contributing to the background chemiluminescence, reproduced in part in Fig. 1, which emits light from approximately 340 nm to 650 nm [4], unlike other important excited-state species such as OH^* and CH^*, which exhibit distinct spectroscopic features. On the other hand, other studies often contribute the background emission over much the same wavelength region to chemiluminescence from CH_2O^* and HCO^*, also depicted approximately in Fig. 1. Although several works have studied CO_2^* chemistry [4–13], a detailed reaction mechanism for the formation and destruction of CO_2^* does not exist, and arguably CO_2^* chemical kinetics are not as well studied as OH^* and CH^* kinetics. Therefore the primary focus of the present study was to verify specific wavelengths that isolate the CO_2^* chemiluminescence, develop a working chemical kinetics mechanism for CO_2^*, and compare this mechanism to new shock-tube results.

This broadband background has been a subject of several studies [4, 14–17], including one in which Dean et al. [18] employed $H_2/N_2O/CO/Ar$ mixtures to measure the rate constant of the reaction $H + N_2O \rightleftarrows N_2 + OH^*$. As Fig. 2 shows, the predicted time histories of the various chemiluminescence species in their mixture show very unique characteristics, making it an ideal vehicle to zero in on a particular species, such as CO_2^*, to study its behaviors and learn more about its broadband characteristics. For example, the peak concentrations of OH^*, CO_2^*, and CH_2O^* occur at noticeably different times; and the shapes of the profiles are rather wide and can have more than one feature, as in OH^* and CO_2^*. In addition to the unique time histories, the Dean et al. mixture of $0.0005H_2 + 0.01N_2O + 0.03CO + 0.9595Ar$ is also ideal because (using the model presented below) the CO_2^* concentration at the conditions of the present study is predicted to be about six orders of magnitude larger than the concentration of both HCO^* and CH_2O^*, making it highly unlikely that photons from the latter two species could be detected, thus isolating CO_2^*. Note that the profiles in Fig. 2 are a result of the first-generation CO_2^* and CH_2O^* mechanism which is discussed in further detail later on, but presented here to illustrate the reasoning for selecting this particular mixture.

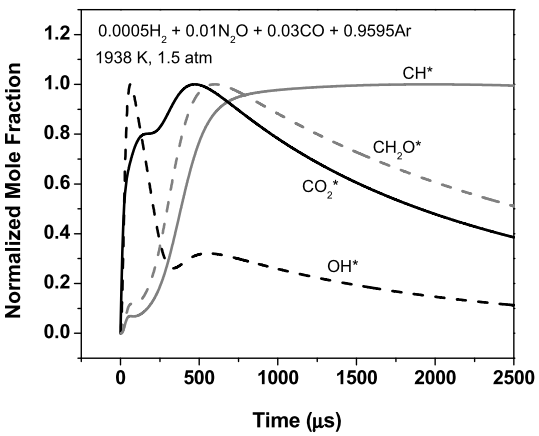

Fig. 2 Model predictions for various chemiluminescence species in $0.0005H_2 + 0.01N_2O + 0.03CO + 0.9595Ar$ at 1938 K and 1.5 atm. This mixture is based on the mixture first used by Dean et al. [18]

Presented in this paper is first a description of the experimental setup, followed by a brief discussion of the kinetics modeling. The experimental results in the form of normalized peak values, time histories, and characteristic times are presented and discussed, along with corresponding comparisons to the kinetics model.

2 Experimental setup

The experiments for this work were performed in a stainless steel shock-tube facility at Texas A&M University. The driven section length and internal diameter are 4.72 m and 15.24 cm, respectively. The driver section is 2.46 m in length with a 7.62-cm internal diameter. Further details on this shock tube can be found in the work of Aul [19]. Standard 1-D shock relations were used to determine the test conditions behind the reflected shock wave. Five PCB-P113A pressure transducers mounted flush with the inner surface of the driven section of the shock tube were used to calculate the incident-shock velocity using four Fluke PM 6666 time-interval counters. The final shock velocity was then extrapolated to the endwall location. Uncertainty in temperature using this method is below 10 K [20]. High-purity gases (H_2, Ar—99.999 %, CO—99.9 %, N_2O—99.5 %) were used to manometrically prepare the mixtures in a stainless steel mixing tank equipped with a perforated stinger along the center of the tank to allow for rapid, turbulent mixing. The mixture utilized for all experiments was the one mentioned above, $0.0005H_2 + 0.01N_2O + 0.03CO + 0.9595Ar$.

Chemiluminescence light emission was collected simultaneously through two sapphire windows located 1.6 cm from the endwall at sidewall locations on both sides of the shock tube. The light from each side then passed through optical filters housed in a custom-made enclosure outside of Hamamatsu 1P21 photomultiplier tubes (PMT), capturing the emission from each test. The dual optical setup allowed for simultaneous emission measurements using two different optical filters. To compare the signals from the two CO_2^* wavelengths, each experimental condition was run twice: once with a 415-nm and a 307-nm optical filter on either side of the shock tube, and then with a 458-nm and a 307-nm optical filter on either side of the shock tube. This method was chosen so that the OH^* chemiluminescence (307 nm) could serve as an anchor for comparing the signals from the two CO_2^* optical filters (415 and 458 nm). Constant optical settings within each experimental set were maintained to allow for direct comparison of the emission profiles from test to test.

3 Chemical kinetics modeling

The baseline mechanism used in this work was from the recent work of Levacque et al. [21], which incorporates the H_2–O_2 chemistry from the National University of Ireland, Galway (NUIG) [22, 23] as well as the OH^* sub-mechanism from Hall and Petersen [24, 25]. Although there are several other validated ground state mechanisms for the H_2–O_2 system, the NUIG C4 mechanism was ultimately chosen because it has shown better agreement over a wider range of mixtures, temperatures, and pressures and has been validated using data from the authors over the last several years.

The mechanism for CO_2^* was produced in three steps. First, thermodynamic calculations were done to identify all the reactions that were energetic enough to produce CO_2^*. For every reaction containing CO_2, the heat of reaction (H_R) was calculated. This heat of reaction was then compared to the energy difference ΔE between CO_2 and CO_2^*, which can be calculated using the following relation:

$$\Delta E = \frac{hc}{\lambda} N_A \tag{1}$$

where h is Planck's constant (6.626×10^{-34} J·s), c is the speed of light (3×10^8 m/s), λ is the wavelength of the chemiluminescence transition, and N_A is Avogadro's number (6.022×10^{23} mol^{-1}). Since CO_2^* is present at wavelengths between 340 and 650 nm, an average wavelength of 495 nm was used for these calculations. The reactions in which the heat of reaction exceeded the energy difference between CO_2 and CO_2^* were then identified as energetic enough to produce CO_2^*.

Once the most likely reactions were identified, their Arrhenius rate coefficients were chosen to be the same as those from their corresponding ground state reactions. The rate coefficients were taken from the GRI 3.0 mechanism; as shown below, most of the reactions ultimately have little effect on the CO_2^* formation, so the choice of either the NUIG C4 or GRI 3.0 rates made little difference to the results. In addition, CO_2^* consumption reactions were included. These reactions and their rates were copied from equivalent reactions from the OH^* consumption reactions from Hall and Petersen [24, 25] along with their Arrhenius rate coefficients, as a first approximation. We realize the limitations of such an estimate, which should be improved upon in future studies. The resulting reaction mechanism for CO_2^* is shown in Table 1.

The last step was to develop new thermodynamic data for CO_2^*. These thermodynamic data are most commonly in the form of the well-known three (i.e., specific heat, enthalpy, and entropy, respectively) following polynomial fits:

$$\frac{c^\circ_{p,k}}{R} = a_{1k} + a_{2k}T_k + a_{3k}T_k^2 + a_{4k}T_k^3 + a_{5k}T_k^4, \tag{2}$$

$$\frac{H^\circ_k}{RT_k} = a_{1k} + \frac{a_{2k}}{2}T_k + \frac{a_{3k}}{3}T_k^2 + \frac{a_{4k}}{4}T_k^3 + \frac{a_{5k}}{5}T_k^4 + \frac{a_{6k}}{T_k}, \tag{3}$$

Table 1 Reaction mechanism for CO_2^*. Units are cal, cm, mole, sec, and K

	Reaction	A	β	E
Formation reactions				
1	$CO + O(+M) \rightleftharpoons CO_2^*(+M)$	1.80E+10	0	2384
	LOW	1.35E+24	−2.788	4191
Efficiency Factors: H_2 2, O_2 6, H_2O 6, AR 0.5, CO 1.5, CO_2 3.5, CH_4 2, C_2H_6 3, He 0.5				
2	$CH_3CHCO + OH \rightleftharpoons C_2H_5 + CO_2^*$	1.17E+12	0	−1010
3	$HCO + O \rightleftharpoons CO_2^* + H$	3.00E+13	0	0
4	$H + H + CO_2 \rightleftharpoons H_2 + CO_2^*$	5.50E+20	−2	0
5	$CH_2 + O_2 \rightleftharpoons CO_2^* + H + H$	2.64E+12	0	1500
Consumption reactions				
6	$CO_2^* + AR \rightleftharpoons CO_2 + AR$	5.20E+10	0.5	0
7	$CO_2^* + H_2O \rightleftharpoons CO_2 + H_2O$	5.92E+12	0.5	−861
8	$CO_2^* + CO_2 \rightleftharpoons CO_2 + CO_2$	2.75E+12	0.5	−968
9	$CO_2^* + CO \rightleftharpoons CO_2 + CO$	3.23E+12	0.5	−787
10	$CO_2^* + H \rightleftharpoons CO_2 + H$	1.50E+12	0.5	0
11	$CO_2^* + H_2 \rightleftharpoons CO_2 + H_2$	2.95E+12	0.5	−444
12	$CO_2^* + O_2 \rightleftharpoons CO_2 + O_2$	2.10E+12	0.5	−482
13	$CO_2^* + O \rightleftharpoons CO_2 + O$	1.50E+12	0.5	0
14	$CO_2^* + OH \rightleftharpoons CO_2 + OH$	1.50E+12	0.5	0
15	$CO_2^* + CH_4 \rightleftharpoons CO_2 + CH_4$	3.36E+12	0.5	−635
16	$CO_2^* \rightleftharpoons CO_2 + h\nu$	1.40E+06	0	0

Table 2 Reaction mechanism for CH_2O^*. Units are cal, cm, mole, sec, and K

	Reaction	A	β	E
Formation reactions				
1	$HO_2 + CH_2 \rightleftharpoons OH + CH_2O^*$	2.00E+13	0	0
2	$OH + CH_3O \rightleftharpoons H_2O + CH_2O^*$	5.00E+12	0	0
3	$HCO + H(+M) \rightleftharpoons CH_2O^*(+M)$	1.09E+12	0.45	−260
	LOW	1.35E+24	−2.57	1425
TROE: $\alpha = 0.7824$, $T^{***} = 271$, $T^{*} = 2755$, $T^{**} = 6570$				
Efficiency factors: H_2 2, H_2O 6, AR 0.7, CO 1.5, CO_2 2, CH_4 2, C_2H_6 3				
4	$C_2H_3 + O_2 \rightleftharpoons HCO + CH_2O^*$	1.70E+29	−5.312	6503
5	$OH + CH_2 \rightleftharpoons CH_2O^* + H$	2.00E+13	0	0
6	$CH_3O + CH_3O \rightleftharpoons CH_3OH + CH_2O^*$	6.03E+13	0	0
7	$CH_3O + CH_3 \rightleftharpoons CH_2O^* + CH_4$	1.20E+13	0	0
8	$HCO + HCO \rightleftharpoons CH_2O^* + CO$	1.80E+13	0	0
9	$CH_3O + H \rightleftharpoons CH_2O^* + H_2$	2.00E+13	0	0
10	$CH_3 + OH \rightleftharpoons CH_2O^* + H_2$	8.00E+09	0.5	−1760
11	$CH_2(s) + OH \rightleftharpoons CH_2O^* + H$	3.00E+13	0	0
12	$CH_2(s) + CO_2 \rightleftharpoons CH_2O^* + CO$	1.40E+13	0	0
13	$CH_2(s) + H_2O \rightleftharpoons CH_2O^* + H_2$	6.82E+10	0.25	−935
Consumption reactions				
14	$CH_2O^* + AR \rightleftharpoons CH_2O + AR$	5.20E+10	0.5	0
15	$CH_2O^* + H_2O \rightleftharpoons CH_2O + H_2O$	5.92E+12	0.5	−86.1
16	$CH_2O^* + CO_2 \rightleftharpoons CH_2O + CO_2$	2.75E+12	0.5	−96.8
17	$CH_2O^* + CO \rightleftharpoons CH_2O + CO$	3.23E+12	0.5	−78.7
18	$CH_2O^* + H \rightleftharpoons CH_2O + H$	1.50E+12	0.5	0
19	$CH_2O^* + H_2 \rightleftharpoons CH_2O + H_2$	2.95E+12	0.5	−44.4
20	$CH_2O^* + O_2 \rightleftharpoons CH_2O + O_2$	2.10E+12	0.5	−48.2
21	$CH_2O^* + O \rightleftharpoons CH_2O + O$	1.50E+12	0.5	0
22	$CH_2O^* + OH \rightleftharpoons CH_2O + OH$	1.50E+12	0.5	0
23	$CH_2O^* + CH_4 \rightleftharpoons CH_2O + CH_4$	3.36E+12	0.5	−63.5
24	$CH_2O^* \rightleftharpoons CH_2O + h\nu$	1.40E+06	0	0

$$\frac{S_k^\circ}{R} = a_{1k}\ln(T_k) + a_{2k}T_k + \frac{a_{3k}}{2}T_k^2 + \frac{a_{4k}}{3}T_k^3 + \frac{a_{5k}}{4}T_k^4 + a_{7k} \quad (4)$$

The seven coefficients (a_{1-7}) for each species k are used to determine their unique thermodynamic properties, c_p, H°, and S°, normalized by the universal gas constant, R. These coefficients are specified for two temperature ranges: 300–1000 K and 1000–5000 K, making up 14 coefficients total.

For CO_2^*, it was assumed that its entropy and constant pressure specific heat were the same as for ground state CO_2. Making this assumption, a_6 was the only coefficient that needed to be calculated for both temperature ranges. First, the enthalpy of formation for CO_2^* ($\Delta H_{f,CO_2}$) was calculated by adding the energy difference between CO_2 and CO_2^* (from Eq. (1)) to the enthalpy of ground state CO_2. Then a_6 for each temperature range was calculated by iteratively changing the coefficient until the calculated H°/RT from Eq. (3) equaled $\Delta H_{f,CO_2}/RT$. A temperature of 300 K was used for finding the low-temperature range coefficient, and 1000 K was used for the high-temperature range coefficient. After the iterations, a low-temperature range coefficient of -3.74×10^2 was determined, and the high-temperature range coefficient was -1.03×10^3. The remaining thermodynamic coefficients used for CO_2^* were the same as those for CO_2.

The mechanism for CH_2O^* was constructed in the same fashion as for CO_2^*. For the energy difference between CH_2O and CH_2O^*, an average wavelength of 430 nm was used, as CH_2O^* is present between about 340 and 520 nm. The thermodynamic coefficient, a_6, for CH_2O^* was calculated as 1.891×10^4 for the low-temperature range and 1.918×10^4 for the high-temperature range. The resulting reaction mechanism for CH_2O^* is shown in Table 2.

It should be noted that this methodology does not necessarily provide the final mechanism set, but it offers a starting point from which to improve upon. A sensitivity analysis and rate of production analysis were done for CO_2^* at a

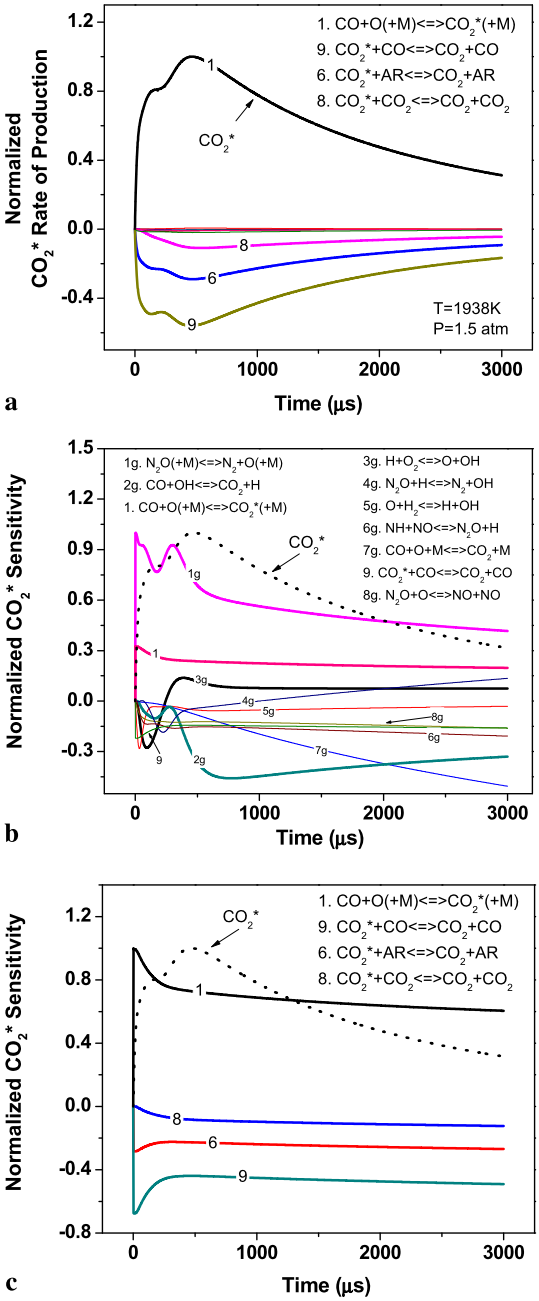

Fig. 3 CO_2^* rate of production (**a**) and sensitivity (**b**), (**c**) analyses at 1938 K and 1.5 atm. (**b**) shows the top 10 reactions sensitive to CO_2^* including ground state chemistry, and (**c**) shows the top 4 reactions exclusive to those containing CO_2^*

representative condition of 1938 K and 1.5 atm for the mixture studied in this work, shown in Fig. 3. Reaction numbers correspond to those listed in Table 1, and "g" represents a ground state reaction. The main reaction that goes to forming CO_2^* at these conditions is the following:

$$CO + O(+M) \rightleftarrows CO_2^*(+M) \quad \text{(R1)}$$

which is shown in the rate of production analysis (Fig. 3a). This result is in agreement with Broida and Gaydon [26]. The rate of production analysis also shows that the main reactions that go toward depleting CO_2^* are as follows:

$$CO_2^* + CO \rightleftarrows CO_2 + CO \quad \text{(R9)}$$

$$CO_2^* + Ar \rightleftarrows CO_2 + Ar \quad \text{(R6)}$$

$$CO_2^* + CO_2 \rightleftarrows CO_2 + CO_2 \quad \text{(R8)}$$

Figure 3b shows that the top ten reactions that are most sensitive toward forming CO_2^* do not all contain CO_2^* as a reactant or product. For example, the following two reactions, along with (R1) above, have rate coefficients that are very sensitive to the formation of CO_2^*:

$$N_2O + M \rightleftarrows N_2 + O + M \quad \text{(R1g)}$$

$$H + O_2 \rightleftarrows OH + O, \quad \text{(R3g)}$$

while the reaction rate of the following reaction is most important for the removal of CO_2^*:

$$CO + OH \rightleftarrows CO_2 + H \quad \text{(R2g)}$$

This result indicates that CO_2^* does in fact depend on ground state chemistry and not entirely on the chemiluminescence sub-mechanism. Similar results have been observed for other chemiluminescence species such as OH^* [25]. Figure 3c shows the most sensitive reactions when the ground state chemistry is disregarded, which are in accordance with the rate of production analysis. Similar results to those shown in Fig. 3 are seen at higher pressure. Based on these results, the working mechanism can be refined such that some of the less important reactions can be removed, and the focus can move toward improving the reaction rates of the more important reactions, such as (R1). Specific comparisons with the new data obtained under the current study are provided in the following section.

4 Results and discussion

The first objective was to compare the experimental results from the two CO_2^* filters to make sure that they were in fact both capturing emission from the same molecule. This comparison was done by using the OH^* profile from each experiment as an anchor for analyzing the CO_2^* signal, in which the peak signal from the CO_2^* filter was divided by the peak signal from the OH^* filter for each experiment. To compare the results from the two experimental sets, these peak levels were normalized to the peak at a common temperature. Figure 4 presents the peak emission over the range of temperature studied, showing good agreement between the experimental sets using the 415-nm filter and the 458-nm filter. This agreement helps to confirm that these two optical

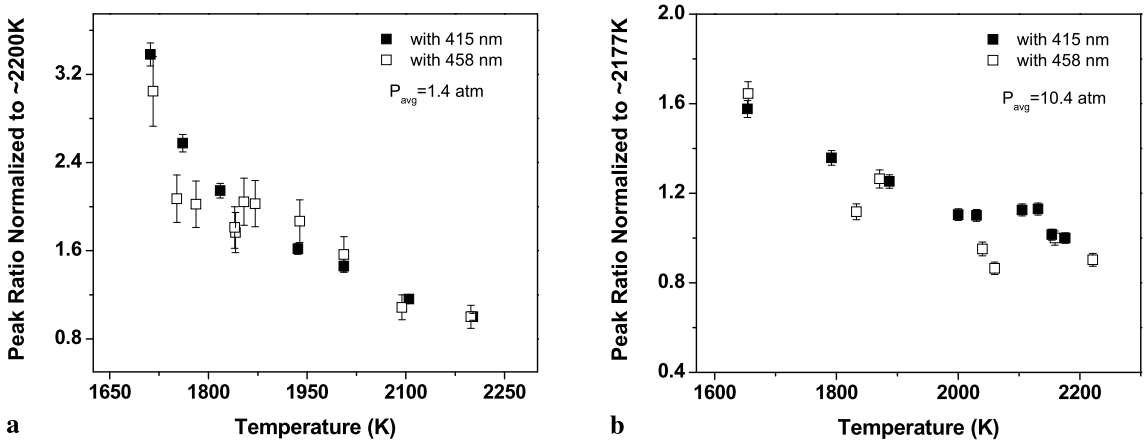

Fig. 4 Experimental results comparing peak signals from the two CO_2^* optical filters anchored by the peak OH^* signal, normalized to a common temperature (2200 and 2177 K) for average pressures of (**a**) 1.4 atm and (**b**) 10.4 atm

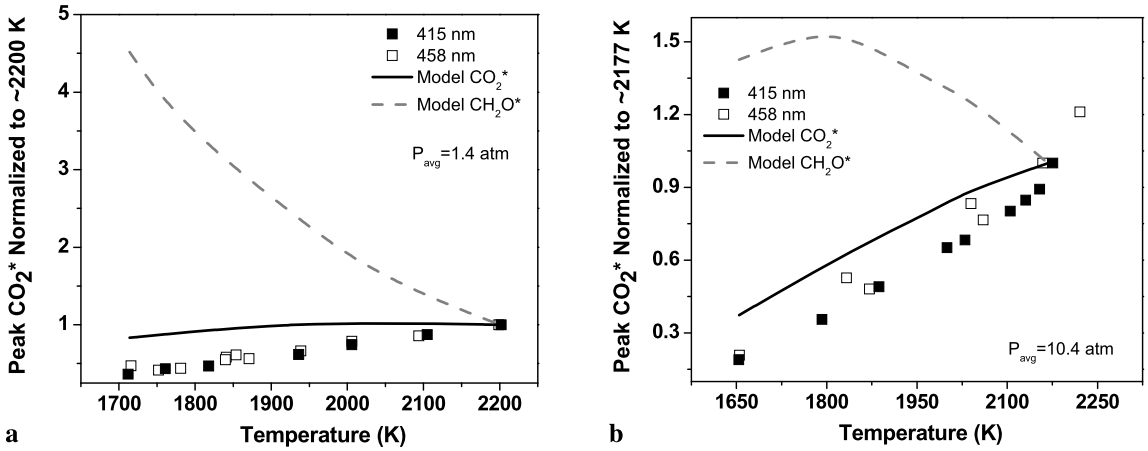

Fig. 5 Peak CO_2^* normalized to common temperature compared with CO_2^* and CH_2O^* mechanism predictions for average pressures of (**a**) 1.4 atm and (**b**) 10.4 atm

filters, centered at 415 nm and 458 nm, are both capturing emission from the same molecule for this mixture. Experimental uncertainty was attributed mostly to the signal-to-noise ratio from the PMT measurements.

The next objective was to verify that CO_2^* was in fact the species being captured in the experiment and not another background species such as CH_2O^*. Model comparisons were made for both pressure sets and are shown in Fig. 5. The peak from each experimental set was normalized to a common temperature for that set to allow for comparison within the two sets and with the chemical kinetics model. As seen in Fig. 5, the CO_2^* model results agree best with the experiment. Therefore, CH_2O^* was ruled out as being a possible background species in this mixture, at least at the two wavelengths utilized (Fig. 8 discussed below also confirms this). Calculations for CH^* were also made, but it too was ruled out since its peak magnitude was around ten orders of magnitude less than CO_2^*, so it is unlikely that the experimental setup employed herein could even capture any CH^* at these conditions. Also, as mentioned above, the peak magnitude of CH_2O^* is predicted to be around six orders of magnitude less than that of CO_2^*, further verifying that any contributions of it to the measured signals can be ruled out.

Figure 6 shows the same data as Fig. 5, but with only the CO_2^* model predictions, to better emphasize the comparison between model and experiment. As shown, the present model overpredicts the peak CO_2^* in both cases, more so for the 1-atm case. However, it does seem to capture the general trend with temperature for the 10.4-atm case.

Agreement between the two CO_2^* filters is ever further verified in the time histories of the emission profiles, shown in Fig. 7. For each experimental set, the normalized traces for both species, OH^* and CO_2^*, lie directly on top of each other, as shown in these representative cases; the results at the other measured temperatures were similar. Also shown in Fig. 7 are the normalized OH^* and CO_2^* mole fractions

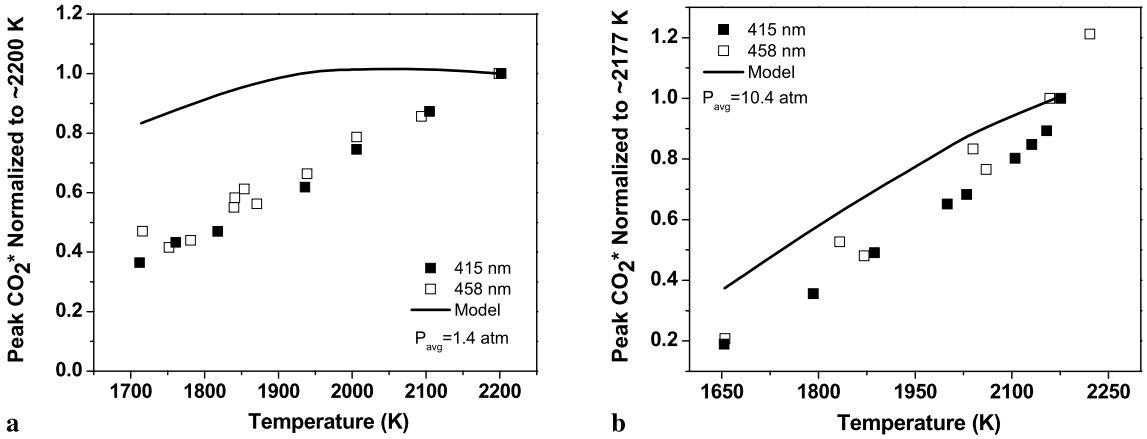

Fig. 6 Peak CO_2^* normalized to common temperature compared with CO_2^* mechanism predictions for average pressures of (**a**) 1.4 atm and (**b**) 10.4 atm

from the mechanism described above, compared to the measurements. Agreement between experiment and model is not perfect, but the mechanism does pick up some of the subtle features in both the OH^* and the CO_2^* species profiles, like in (a)–(c) of Fig. 7. The exact timing or shape may not agree, but the fact that the mechanism does pick up on some of these subtleties is promising. It should also be noted that all model results were anchored to the peak OH^* to allow for timing comparisons between the two species; that is, the CO_2^* and OH^* profiles from the model predictions were both time shifted such that the OH^* peak from the mechanism matched the OH^* peak from the experiment. In this way, the predicted shape of the time history profile is emphasized independently from the model's prediction of the ignition delay time for each experiment.

Figure 8 shows predictions of the two working mechanisms for CO_2^* and CH_2O^* compared to the time history of the experiment from one of the CO_2^* filters for a representative case at both pressures. Only one of the CO_2^* filters is shown here since both CO_2^* filters were shown to produce the same result (Fig. 7). As Fig. 8 shows, the agreement is noticeably better with the CO_2^* mechanism. It should be noted that the time shift for both CO_2^* and CH_2O^* is in accordance with Fig. 7. At lower pressures (Fig. 8a), the CO_2^* mechanism picks up the features of the experimental profile better than the CH_2O^* mechanism, as seen in the height of the first rise relative to the peak. At higher pressures (Fig. 8b), the model predicts CH_2O^* to occur much later than CO_2^*, and the experiment does not show the incipient rise seen in the CH_2O^* prediction. This difference in timing between CO_2^* and CH_2O^*, in conjunction with the peak magnitude comparisons (Fig. 5), further confirms that CH_2O^* can be neglected at these conditions and that the species being measured at the two chosen wavelengths is CO_2^*.

To further test the working CO_2^* mechanism, the time-to-peak, τ_p, was determined from the experiment for both OH^* and CO_2^* and compared to the model. Note that a time-to-peak is probably a better marker for the time dependence than an ignition delay time for the rather exotic mixture used in the present study; the latter is difficult to define from the OH^* and CO_2^* time histories. Figure 9 shows the results on Arrhenius-type plots that give the time-to-peak on a log scale as a function of inverse temperature for average pressures of (a) 1.4 atm and (b) 10.4 atm. In general, the model underpredicts τ_p, more so for CO_2^* at 10.4 atm. This type of analysis can provide further insight into improvements to the ground state mechanism; note that changes to the chemiluminescence sub-mechanisms (Tables 1 and 2) have virtually no effect on the time-to-peak, so such information can be used for improving the H_2-CO-NO_x chemistry in the baseline mechanism. It should also be noted that the results in Fig. 9 from the two experimental sets (indicated by closed and open symbols) show good agreement, further confirming that the same species are being measured at both wavelengths.

Slack and Grillo [7] suggested a rate for (R1), which is compared with the experimental results and the working CO_2^* mechanism from the present paper in Figs. 10 and 11. Also shown is the product of CO and O concentration, [CO][O], which has been shown to be proportional to CO_2^* chemiluminescence [14]. In Fig. 10, the product of [CO] and [O] shows very good agreement with the data, while the rate from [7] overpredicts the peak for both pressure sets, more so than the working CO_2^* mechanism in this study. There is little noticeable difference in the time history of CO_2^* (Fig. 11), further verifying that the CO_2^* submechanism is more influential on the peak CO_2^* magnitude, and overall time history is more dependent on the ground state mechanism.

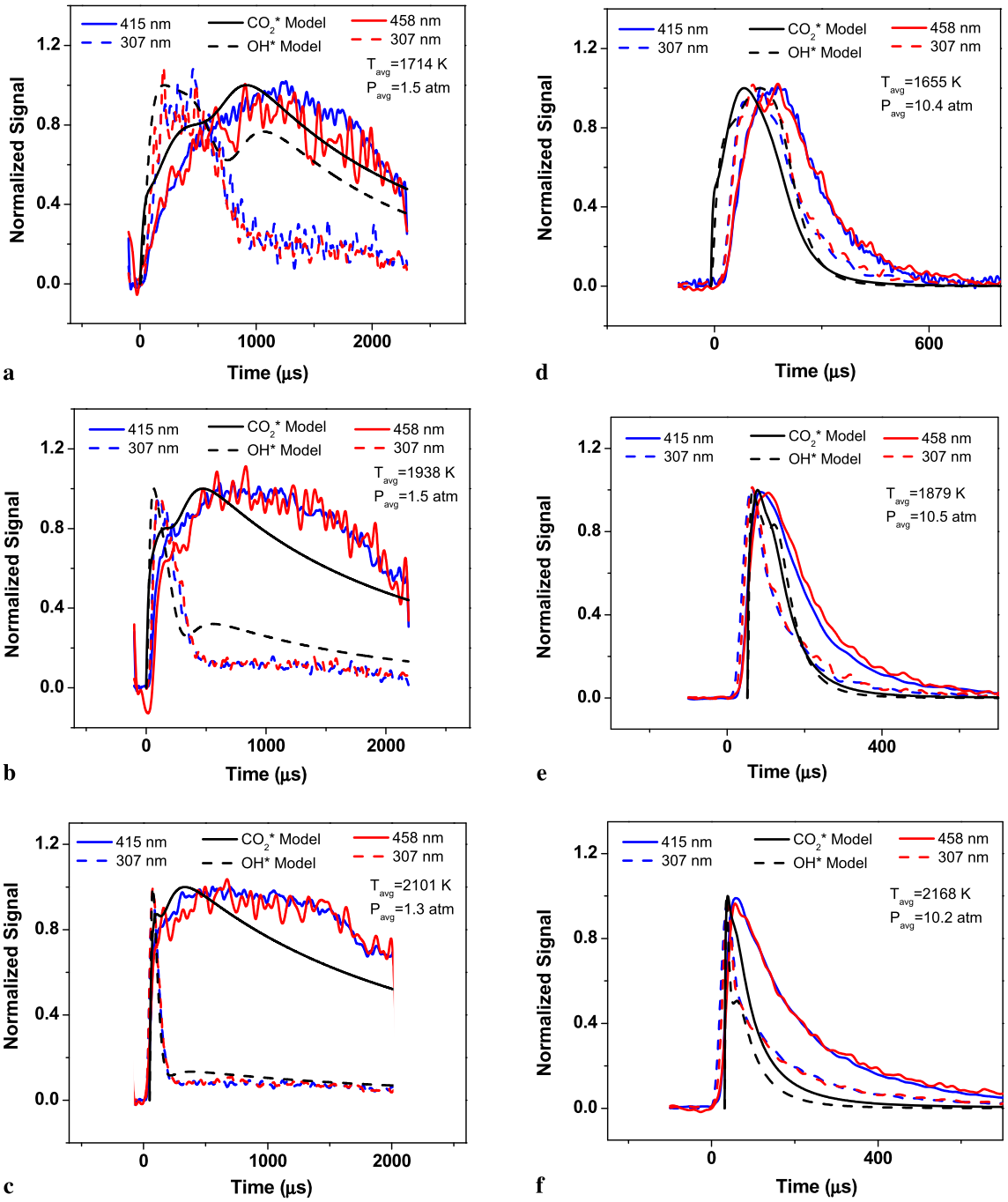

Fig. 7 Normalized OH^* and CO_2^* experimental profiles compared with model results for low, medium, and high temperature at (**a**)–(**c**) low pressure and (**d**)–(**f**) high pressure

5 Conclusions and future work

Shock-tube experiments were performed in $H_2/N_2O/CO/Ar$ mixtures at low and elevated pressures to assess the ability of a first-generation CO_2^* mechanism to predict measured trends. Two experimental sets were performed using a dual optical setup which measured chemiluminescence from OH^* as the baseline compared with the emission through two different CO_2^* filters, one centered at 415 nm and one at 458 nm. The results of these experiments confirmed that both filters were in fact capturing the same CO_2^* signal, which was then compared to the model predictions.

A working mechanism for CO_2^* and CH_2O^* was produced and compared with the experimental results, which ruled out CH_2O^* as being present at measurable levels at these conditions. More extensive comparisons were then

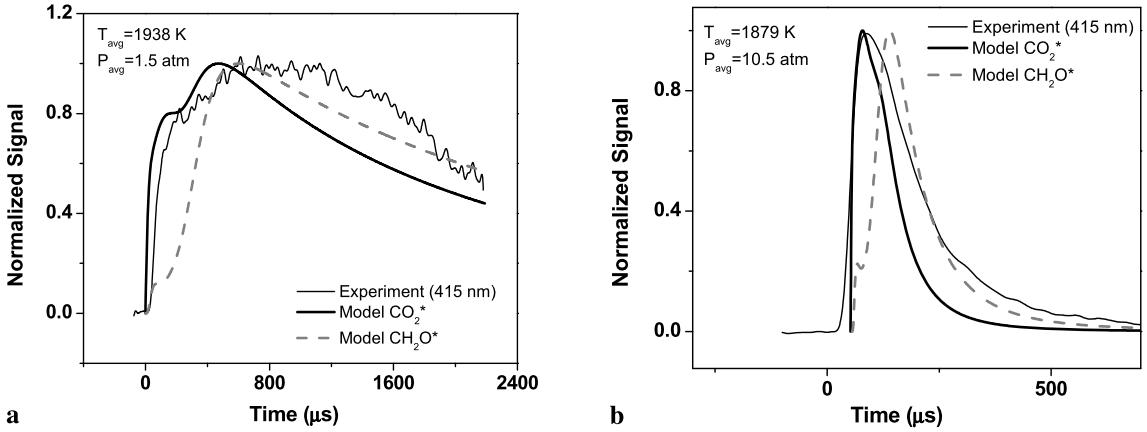

Fig. 8 Representative low (**a**) and high (**b**) pressure experimental CO_2^* time histories compared with the working CO_2^* and CH_2O^* mechanisms

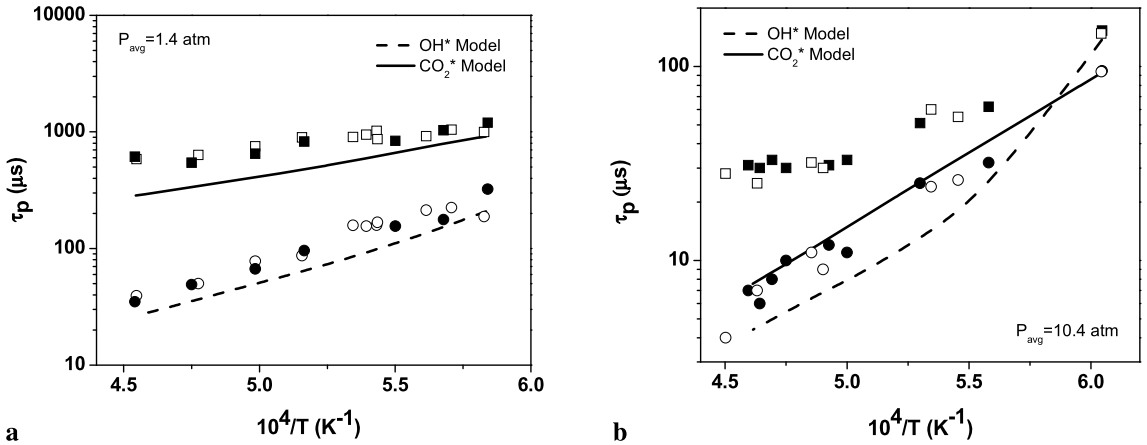

Fig. 9 Time-to-peak data and modeling at average pressures of (**a**) 1.4 atm and (**b**) 10.4 atm Square symbols are the CO_2^* data, and circles are the OH^* data. *Open* and *closed symbols* correspond to the two experimental sets at each condition (458- and 415-nm filters, respectively)

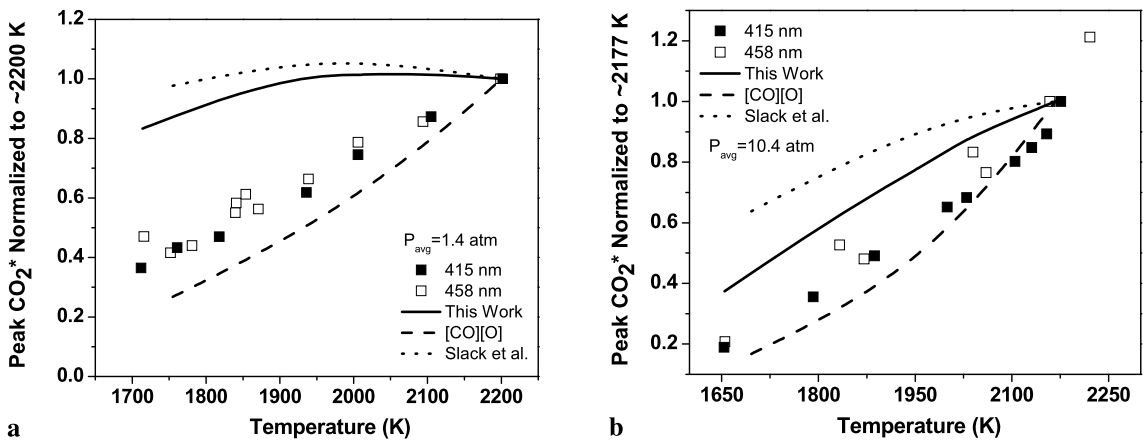

Fig. 10 Alternate peak CO_2^* predictions from another rate in the literature and the product of [CO] and [O] compared with the working model and experimental results from this work for average pressures of (**a**) 1.4 atm and (**b**) 10.4 atm

made for CO_2^* in terms of species time histories, the temperature dependence of peak CO_2^* magnitude, and time-to-peak formation. The mechanism tended to underpredict time-to-peak for both CO_2^* and OH^*. The time history comparisons showed that the mechanism does pick up on some of the subtle features in the species profiles, however agreement is

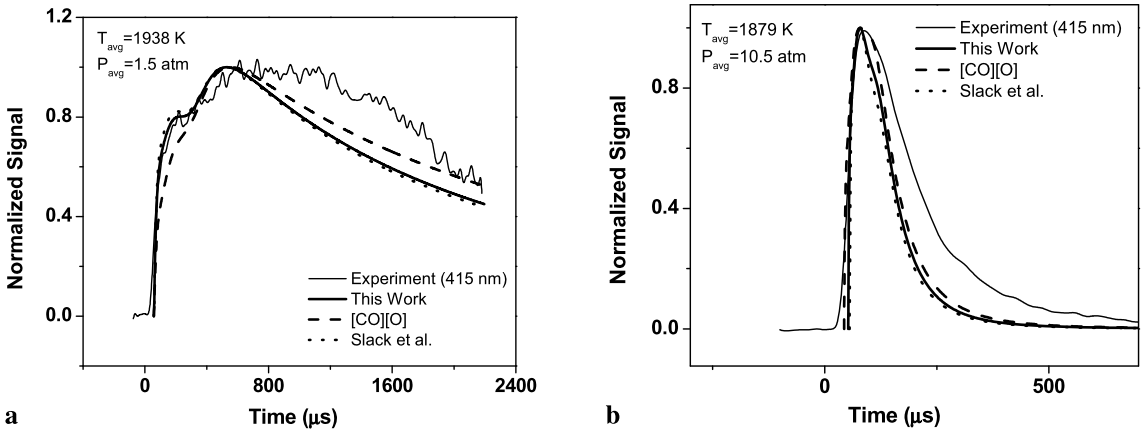

Fig. 11 Alternate CO_2^* time history predictions from another rate in the literature and the product of [CO] and [O] compared with the working model and experimental results from this work for a low (**a**) and high (**b**) pressure case

not perfect, and improvements to the mechanism can still be made in that regard. The model also overpredicts peak CO_2^* for both pressure sets and fails to capture the trend with temperature at low pressures. This problem in predicting the peak intensity will most likely require changes to the CO_2^* sub-mechanism, and not the overall baseline mechanism, which has more influence on the time history shape of the species rather than the peak magnitude.

Ongoing work is being conducted on the mechanism of Levacque et al. [21], which could lead to better agreement in species time histories and time-to-peak. Further improvements to the CO_2^* sub-mechanism are also underway to address the peak magnitude disagreements.

Acknowledgements This work was supported primarily by Alstom Power, Baden, Switzerland. Additional support came from the National Science Foundation under grant number EEC-1004859.

References

1. E.L. Petersen, M.M. Kopp, N.S. Donato, F. Güthe, J. Eng. Gas Turbines Power **134**, 051501 (2012)
2. M. Lauer, T. Sattelmayer, J. Eng. Gas Turbines Power **132**, 061502 (2010)
3. E. Mancaruso, B.M. Vaglieco, Fuel **90**, 511 (2011)
4. S.B. Gupta, B.P. Bihari, M.S. Biruduganti, R.R. Sekar, J. Zigan, Proc. Combust. Inst. **33**, 3131 (2011)
5. V.N. Nori, J.M. Seitzman, AIAA Paper 2007-0466 (2007)
6. V.N. Nori, J.M. Seitzman, AIAA Paper 2008-953 (2008)
7. M. Slack, A. Grillo, Combust. Flame **59**, 189 (1985)
8. B.F. Myers, E.R. Bartle, J. Chem. Phys. **47**, 1783 (1967)
9. C.J. Malerich, J.H. Scanlon, Chem. Phys. **110**, 303 (1986)
10. C. Rond, A. Bultel, P. Boubert, B.G. Chèron, Chem. Phys. **354**, 16 (2008)
11. A. Vesel, M. Mozetic, A. Drenik, M. Balat-Pichelin, Chem. Phys. **382**, 127 (2011)
12. A.M. Pravilov, L.G. Smirnova, Kinet. Catal. **22**, 832 (1981)
13. D.L. Baulch, D.D. Drysdale, J. Duxbury, S.J. Grant, Evaluated Kinetic Data for High Temperature Reactions, vol. 3 (1976)
14. J.M. Samaniego, F.N. Egolfopoulos, C.T. Bowman, Combust. Sci. Technol. **109**, 183 (1995)
15. B. Higgins, M.Q. McQuay, F. Lacas, J.C. Rolon, N. Darabiha, S. Candel, Fuel **80**, 67 (2011)
16. Y. Ikeda, J. Kojima, H. Hashimoto, T. Nakajima, AIAA paper 2002-0191 (2002)
17. F.V. Tinaut, M. Reyes, B. Giménez, J.V. Pastor, Energy Fuels **25**, 119 (2011)
18. A.M. Dean, D.C. Steiner, E.E. Wang, Combust. Flame **32**, 73 (1978)
19. C.J. Aul, M.S. Thesis, Texas A&M University (2009)
20. E.L. Petersen, M.J.A. Rickard, M.W. Crofton, E.D. Abbey, M.J. Traum, D.M. Kalitan, Meas. Sci. Technol. **16**, 1716 (2005)
21. A. Levacque, O. Mathieu, E.L. Petersen, in Spring Technical Meeting of the Western States Section of the Combustion Institute (2012)
22. D. Healy, M.M. Kopp, N.L. Polley, E.L. Petersen, G. Bourque, H.J. Curran, Energy Fuels **24**, 1617 (2010)
23. D. Healy, H.J. Curran, N.S. Donato, C.J. Aul, E.L. Petersen, C.M. Zinner, G. Bourque, H.J. Curran, Combust. Flame **157**, 1540 (2010)
24. J.M. Hall, E.L. Petersen, AIAA paper 2004-4164 (2004)
25. J.M. Hall, E.L. Petersen, Int. J. Chem. Kinet. **38**, 714 (2006)
26. H.P. Broida, A.G. Gaydon, Trans. Faraday Soc. **49**, 1190 (1953)